IEEE Access
Multidisciplinary | Rapid Review | Open Access Journal

Received 7 May 2024, accepted 27 May 2024, date of publication 11 June 2024, date of current version 24 June 2024.

Digital Object Identifier 10.1109/ACCESS.2024.3412854

RESEARCH ARTICLE

Fingerprinting Database Development Methods for Reconfigurable Intelligent Surface Assisted Indoor Positioning System

AISHA JAVED[1], NAVEED UL HASSAN[1], (Senior Member, IEEE), AMMAR RAFIQUE[2], MUHAMMAD ZUBAIR[2], (Senior Member, IEEE), MARCO DI RENZO[3], (Fellow, IEEE), AND CHAU YUEN[4], (Fellow, IEEE)

[1]Department of Electrical Engineering, Lahore University of Management Sciences (LUMS), Lahore 54792, Pakistan
[2]Electrical Engineering Department, Information Technology University (ITU), Lahore, Punjab 54600, Pakistan
[3]Université Paris-Saclay, CNRS, CentraleSupélec, Laboratoire des Signaux et Systèmes, 3 Rue Joliot-Curie, 91192 Gif-sur-Yvette, France
[4]School of Electrical and Electronics Engineering, Nanyang Technological University, Singapore 639798

Corresponding authors: Naveed Ul Hassan (naveed.hassan@lums.edu.pk), Muhammad Zubair (muhammad.zubair@itu.edu.pk), and Marco Di Renzo (marco.di-renzo@universite-paris-saclay.fr)

This work was supported in part by Lahore University of Management Sciences (LUMS) Faculty Initiative Fund (FIF), and in part by the Information Technology University (ITU) Pre-Doctoral Fellowship. The work of Marco Di Renzo was supported in part by the European Commission through the Horizon Europe project titled "COVER" under Grant 101086228, in part by the Horizon Europe project titled "UNITE" under Grant 101129618, in part by the Horizon Europe project titled "INSTINCT" under Grant 101139161, in part by the Agence Nationale de la Recherche (ANR) through the France 2030 project titled ANR-PEPR Networks of the Future NF-PERSEUS under Grant 22-PEFT-004, and in part by the CHIST-ERA project titled PASSIONATE under Grant CHIST-ERA-22-WAI-04 and Grant ANR-23-CHR4-0003-01. The work of Chau Yuen was supported in part by the Ministry of Education (MOE) Singapore MOE Tier 2 under Award MOE-T2EP50220-0019.

ABSTRACT The positioning accuracy of a reconfigurable intelligent surface (RIS) assisted indoor positioning system (IPS) can be improved by developing a fingerprinting database for different RIS configurations. Every RIS configuration generates a different radio map of the indoor environment such that the variations in the received power are used to localize unknown receivers. However, creating a diverse fingerprinting database is challenging and time consuming. To this end, we compare three end-to-end (E2E) propagation modeling techniques that include a full-wave electromagnetic (EM) simulator-based model (FWS-E2E), and two hybrid models called HYB1-E2E and HYB2-E2E. The FWS-E2E technique models the RIS and the entire indoor environment in a full-wave EM simulator. On the other hand, the hybrid techniques mostly rely on analytical equations while using some important data from the EM simulator. In this paper, we also discuss methods and algorithms to identify useful RIS configurations having the potential to generate diverse radio maps for increasing the positioning accuracy of the IPS. Both hybrid methods significantly reduce the complexity of generating the radio map. Experimental results are also provided to compare the performance of the E2E models.

INDEX TERMS Fingerprinting, IPS, RIS.

I. INTRODUCTION

The problem of localizing a receiver in an indoor space is important because global positioning system (GPS) signals are severely degraded and fail to provide meaningful accuracy for indoor location-based services [1], [2]. WiFi signals are abundantly available in indoor spaces, therefore, radio frequency (RF) based indoor positioning systems (IPS) are more popular than other approaches [3], [4]. However, to achieve high indoor localization accuracy, WiFi fingerprinting is generally required. In WiFi fingerprinting, there is an offline phase and an online phase [5]. In the offline phase, a fingerprinting database of radio maps of the indoor space is created, while in the online phase, this database is used to determine the location of a receiver. During the online phase the received signal strength (RSS) of the received signals is compared with the RSS values already stored in the fingerprinting database and the best match is utilized to

The associate editor coordinating the review of this manuscript and approving it for publication was Ding Xu.

determine the current location of the receiver [6]. A major challenge of any radio frequency (RF) fingerprinting based IPS is the acquisition of a fingerprinting database [7]. Planned RF measurement campaigns, crowdsourcing RF data from indoor space users, and end-to-end (E2E) RF propagation models are utilized to develop a fingerprinting database.

In recent years, reconfigurable intelligent surfaces (RIS) and holographic surfaces have gained significant research attention [8], [9], [10], [11], [12], [13]. An RIS is a thin rectangular array of sub-wavelength elements called unit cells. In an RIS, the states or, equivalently, the phases of the unit cells are collectively controlled and reconfigured [14], [15]. By changing the phases of the unit cells, the received power or the RSS is changed.[1] Suppose an RIS has N unit cells and each unit cell has L discrete states, then this RIS has L^N configurations. At any given point in space, L^N different values of received power can be generated (one value per RIS configuration). For example, a moderately sized RIS with $N = 100$ and $L = 2$ has 2^{100} configurations. Therefore, a very large number of radio maps of a given wireless environment can be created by using a single RIS and a single WiFi router or access point (AP). Thus, RIS integration offers substantial benefits, including savings in infrastructure space and deployment costs. These advantages address prevalent issues in traditional IPS that typically require multiple APs to increase dimensionality. The ability of an RIS to impact the received power at different locations by changing its configuration can be used to build and improve the performance of an IPS [16], [17], [18]. This transformative potential of RIS is further explored in [19], where the authors introduce several model-based approaches for RIS signal processing. Focusing on signal processing aspects such as channel estimation, transmission design, and radio localization, the review highlights how strategic deployment and parameter adjustment of RIS can optimize signal propagation paths. This enhances the accuracy of IPS and opens new avenues for research into using RIS technology for advanced signal processing and positioning solutions.

RIS also emerged as a promising solution for millimeter wave (mmWave) positioning, addressing the challenge of blockage sensitivity and marking a significant advancement toward sixth-generation (6G) wireless systems [20]. This development is part of recent advancements that propose mmWave systems to improve positioning accuracy. However, the full potential and various aspects of RIS-assisted IPS still require extensive investigation to fully understand the potential of this research field. Given the large number of configuration sets and the fact that not all configurations facilitate improved accuracy for RIS-assisted IPS, it is necessary to identify the useful RIS configurations that enhance localization accuracy and to develop a fingerprinting database with these configurations. Moreover, RF measurement campaigns for multiple RIS configurations become labor-intensive and costly, while crowdsourcing methods lack accuracy and reliability. In this context, computationally efficient RF propagation models can support the development of a fingerprinting database with reasonable accuracy [21]. By carefully selecting configurations and using propagation models that effectively simulate the RIS response in the environment, we can reduce the dimensionality of the fingerprinting dataset and utilize the fingerprinting technique to improve IPS accuracy.

This strategic selection of RIS configurations, through parameter adjustments, strongly correlates with the effectiveness of radio maps used in WiFi fingerprinting, which is important for optimizing indoor positioning systems. By adjusting parameters such as the number of unit cells on an RIS, we achieve more precise control over the EM field within a specific environment. This precision in manipulating EM fields enables stronger signal strengths at targeted points, significantly enhancing spatial resolution. Such enhanced resolution allows for the creation of finer and more accurate radio maps, which are crucial in complex and large indoor spaces.

Additionally, the number of states that the unit cells can adopt plays a vital role in shaping the radio maps. More discrete states allow for more precise control and can produce more detailed radio maps, while fewer discrete states simplify the process and reduce system complexity. Therefore, selecting the number of discrete states involves a trade-off. By adjusting these parameters, we can create radio maps that enhance the received signal power at targeted points or boost the received power at specific targets while reducing it at others. This flexibility in radio map generation stems from the interplay of RIS parameters, which directly influence the signal's strength and propagation characteristics. Such adjustments alter the signal power distribution and demonstrate the direct correlation between these parameter changes and the resulting diversity in radio map configurations. To generate radio maps with these desired characteristics, different types of optimization problems need to be formulated and solved. These optimization problems are designed to identify the most effective RIS configurations for enhancing signal strength. Through this approach, we leverage the correlation between radio maps and RIS parameters to create customized and effective solutions for indoor positioning.

Therefore, the integration of RIS into IPS brings several advantages. For instance, optimization algorithms can be employed to select radio maps that can potentially improve localization accuracy. Focusing on configurations that significantly impact localization accuracy makes the process more targeted and efficient, avoiding the exhaustive and impractical approach of considering every possible RIS configuration. This methodical approach highlights the effective alliance between computational models and their practical application, ensuring that RIS technology is utilized optimally to advance the capabilities of IPS. This not only maximizes the potential benefits of RIS but also makes the

[1] In this paper, we use the terms RSS and received power interchangeably.

development and implementation of IPS more efficient and effective.

In this paper, we present methods and algorithms to determine the best RIS configurations for RIS-assisted IPS designs. The indoor locations from where the localization requests are expected to arrive more frequently are identified. For every such location, we determine the best RIS configuration through our algorithms that maximizes the received power at the target point. When the phases of the unit cells are varied in a continuous range, optimal solutions are efficiently obtained by utilizing a gradient-ascent algorithm. On the other hand, when the phases of unit cells are discrete, we use a genetic algorithm (GA) for finding the best RIS configuration. For developing a fingerprinting database with different RIS configurations, we discuss three E2E propagation modeling techniques. These include full-wave electromagnetic (EM) simulator-based E2E modeling (FWS-E2E), and two hybrid models called HYB1-E2E and HYB2-E2E.

In FWS-E2E, the RIS and the complete indoor environment are simulated in a commercially available full-wave simulators such as CST or HFFS. The FWS-E2E model has a very high accuracy in predicting the received power. However, its computational complexity grows exponentially with the size of the indoor environment, and for every new RIS configuration, the simulations have to be rerun. Despite the complexity, FWS-E2E still provides several advantages over RF measurement campaigns. Unlike FWS-E2E modeling, which entirely relies on simulations, the hybrid models use analytical equations and some data from full-wave simulators.

In HYB1-E2E, an analytical equation of the received power is developed with the help of circuit and antenna theories [12], [22]. In the literature, antenna theory is used to model the entire channel responses from the transmitter to RIS, RIS to the receiver, and the self and mutual coupling of the unit cells as appropriate impedances. The resulting circuit model is then used to compute the received power at different indoor locations. In our case, to improve the accuracy of the model, we use a full-wave simulator to determine the self and mutual coupling among the unit cells, hence obtaining a hybrid model. In HYB1-E2E, for a given RIS, this requires only a one-time computational effort in determining the impedances with a full-wave simulator. In HYB2-E2E, we use general path loss models from the literature for RIS-assisted communication systems [23], [24]. Such models include the dependence of the received power on the normalized radiation responses of the transmit antenna, unit cells, and the receive antenna. Therefore, in HYB2-E2E, we obtain the exact radiation responses with the help of a full-wave simulator. Once again, the computation of these responses is a one-time computational effort.

We compare and discuss the relative complexity of the three E2E models for developing a fingerprinting database. We perform numerical simulations for a $10\times10\times3\ m^3$ indoor space with one WiFi router operating at 5.2 GHz assisted by a square 40×40 RIS (1600 unit cells). The received powers at various indoor locations for different RIS configurations obtained for the HYB1-E2E and HYB2-E2E models are compared. We also perform experiments where we measure the RSS values with the help of a locally manufactured 28×27 (756 elements) 1-bit RIS. Thus, in this latter case, we are also able to compare the RSS values obtained from the HYB1-E2E and HYB2-E2E models with experimental results. We note that the algorithms for unit cells with continuous- and discrete-valued phase shifts are able to focus the power at the desired locations. However, as expected, when the phases of the unit cell can be continuously varied, relatively more power can be focused at the target grid point. Overall, the use of realistic impedance and realistic radiation responses in the hybrid models significantly improves the performance. The hybrid models and the algorithms for continuous and discrete valued phase shifts can therefore be used for developing a fingerprinting database for an RIS-assisted IPS.

Focusing on integrating RIS into IPS, this paper addresses challenges and presents solutions for using RIS in positioning systems. We aim to reduce the complexity and cost associated with traditional RF measurement campaigns by developing an optimization algorithm for generating a useful set of configurations coupled with using E2E propagation models. Thus, we establish a solid foundation for future advancements in IPS and the application of learning-based localization algorithms, paving the way for a future where IPS is more efficient, cost-effective, and accurate.

The key contributions of this paper are the following:

- We discuss three E2E propagation modeling techniques for developing a fingerprinting database with different RIS configurations: a FWS-E2E model and two hybrid models (HYB1-E2E and HYB2-E2E). These models are crucial for accurately simulating an indoor environment and RIS behavior, thus facilitating the creation of a comprehensive fingerprinting database for improved IPS accuracy.
- We develop algorithms to determine the optimal RIS configurations that enhance localization accuracy. By employing the gradient-ascent algorithm for continuous adjustable unit cells and the GA for discrete adjustable unit cells, this research provides a methodological framework for maximizing the received power at targeted locations and optimizing RIS-assisted IPS designs.
- Through numerical simulations and practical experiments, the paper compares the effectiveness of the proposed E2E models and optimization algorithms in focusing power at desired locations within an indoor space. This comparative analysis, supported by experimental validation, underscores the potential of the hybrid models and the developed algorithms to significantly improve the performance of RIS-assisted IPS, offering a promising direction for future research in the field.

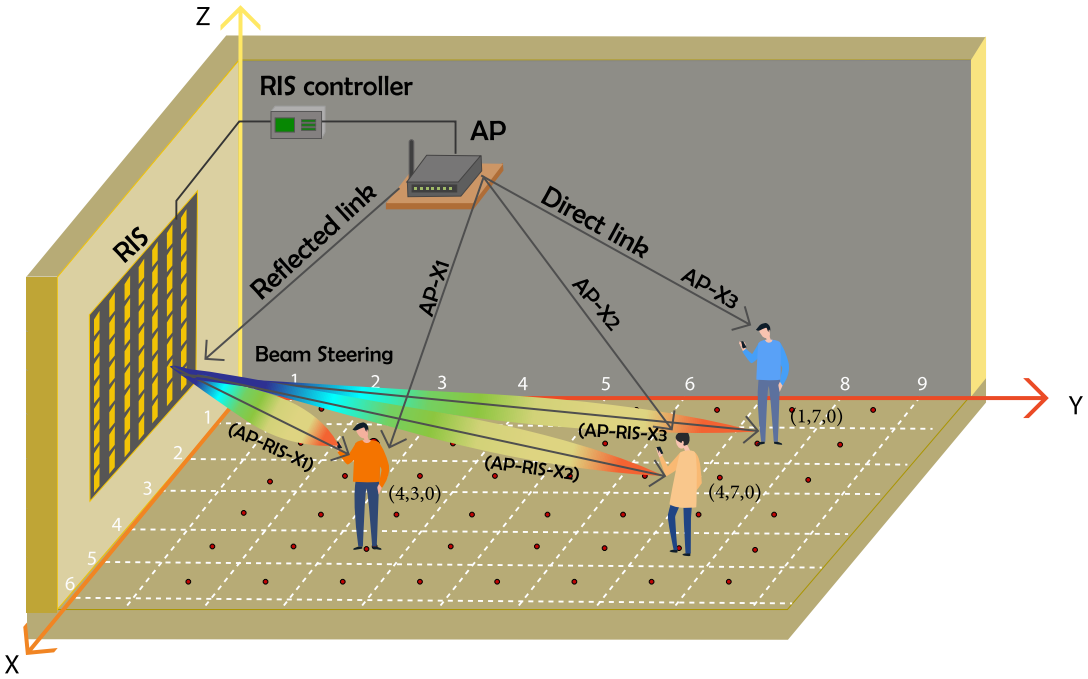

FIGURE 1. RIS-assisted IPS. RIS, WiFi access point (AP) the direct and the reflected signal paths are shown. The indoor space is also divided into a uniformly spaced grid.

The rest of the paper is organized as follows. In Section II, we discuss the RIS-assisted IPS design. In Section III, we present the three E2E models. In Section IV, we discuss the methods and algorithms for selecting the best RIS configurations. In Section V, we present the simulation results. In Section VI, we present the experimental results and complexity comparison. In Section VII, we conclude the paper.

II. RIS-ASSISTED IPS DESIGN

In this paper, we consider an RIS-assisted IPS design. The major components of the system are shown in Figure 1. We assume only one WiFi router. A rectangular RIS consisting of N unit cells is placed on a wall.[2] The unit cell dimensions are always assumed to be less than the operating frequency of the WiFi router. For practical purposes, we also divide the entire indoor space into a set of uniformly spaced grid points. The location coordinates of these grid points are determined with respect to a local coordinate system x-y-z whose origin $(0, 0, 0)$ is conveniently selected. The unknown receiver is localized in this local coordinate system. We assume that an RIS configuration is changed with the help of a suitable controller, for example, a field programmable gate array (FPGA) or a micro-controller. Several unit cell designs are available in the literature [25], [26], [27], [28]. Practical unit cells that use PIN diodes as their control elements offer either 2, 4, or 8 distinct phases [25]. On the other hand, when a unit cell is controlled by varactor diodes, the phase can be continuously varied [29].

[2]The optimal placement of RIS for improving the localization accuracy of IPS design is an interesting research problem. However, this problem is not considered in this paper and it is postponed to a future research work.

For both continuous and discrete valued phase shifts, the total number of RIS configurations exponentially increases with the number of unit cells. In our RIS-assisted IPS design, we are therefore interested in finding the RIS configurations that are helpful in improving the localization accuracy. We also develop a fingerprinting database using these configurations and store it at a localization server. The fingerprinting database contains the labeled RSS values from the grid points. At any grid point X, the received power is the sum of the powers obtained from the direct and the reflected links. The direct link is represented by AP-X (also referred to as line of sight (LoS) link), while the reflected link, which is an RIS-assisted link, is represented as AP-RIS-X (also referred to as non-line of sight (NLoS) or virtual LoS link). In the online phase, when a user requests a localization service, the RIS controller cycles through multiple RIS configurations that are available in the database. The user measures the RSS values from its unknown location and sends these values to the localization server. The online algorithm is run at the server which then compares the received RSS values with the database and comes up with a location estimation.

III. E2E PROPAGATION MODELS FOR AN RIS-ASSISTED IPS DESIGN

By effectively utilizing the numerous configurations offered by the RIS, the performance and localization accuracy of an IPS can be significantly improved. However, the development of a fingerprinting database remains a major limiting factor. To this end, we explore and compare three different approaches called FWS-E2E, HYB1-E2E, and HYB-E2E for determining the received powers in RIS-assisted IPSs with various performance-complexity tradeoffs.

A. FWS-E2E MODELING

The FWS-E2E modeling approach employs a commercially available full-wave EM simulator such as CST or HFSS. These simulators have the ability to solve the EM equations without simplifying assumptions and offer a wide range of time and frequency domain solvers such as the finite element method (FEM), finite integration technique (FIT), and transmission line matrix method (TLM). The choice of the solver (FEM, FIT, TLM) in the FWS-E2E method also depends on the boundary conditions, which can be classified as periodic or aperiodic. Assuming a plane wave source at normal incidence, periodic boundary conditions are applicable. However, when the angle of incidence is not normal or the size of the RIS is smaller than 5λ, to avoid the fringing effects, aperiodic boundary conditions with full structure simulation are required for better accuracy. Periodic boundary conditions simplify the problem and save computational resources. On the other hand, full structure simulation with aperiodic boundary conditions has extremely high computational complexity.

The key steps of the FWS-E2E modeling approach to simulate an RIS-assisted IPS are the following:

1) WiFi router modeling: The specifications of the WiFi router used in the IPS design are used in the antenna simulation module of the software to calculate its radiation pattern.
2) Unit cell modeling: The unit cell is designed in CST for the desired operating frequency. The control element on the unit cell such as the PIN diode is also modeled, usually as a lumped element according to specifications given in the datasheet provided by the manufacturer.
3) RIS modeling: Depending on the number of RIS elements N and the inter-cell distance, which should be less than $\lambda/2$, where λ is the wavelength, the unit cells are arranged in a rectangular planar array to model the RIS.
4) Indoor space modeling: The indoor space is modeled as a 3D box made of 'vacuum' material. The dimensions of the box are adjusted according to the size of the indoor space. The locations of transmit antenna and RIS are specified in the indoor space.
5) Scatterers and structures modeling: Any significant scatterers or structures in the indoor space are also modeled for more realistic indoor spaces.
6) Field monitors placement: We want to observe the E-field in the indoor space at the frequency of the considered WiFi router. Therefore, we place E-field monitors at the desired frequency in the indoor space.
7) RIS configuration selection: The states of all the control elements on the unit cells in the RIS are set according to the desired RIS configuration.
8) Simulation running: After loading the desired RIS configuration, we start the simulation.
9) Received power computation: When the simulation ends, we get the E-field values at the desired locations for the specified RIS configuration. We use these values to compute the received powers and store them in the fingerprinting database.

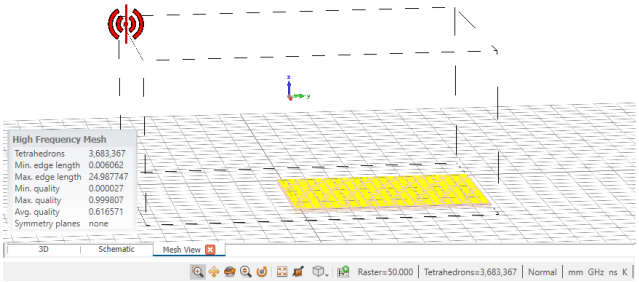

FIGURE 2. Screenshot of a simulation setup in CST microwave studio. The transmit antenna is shown in red, the RIS is shown in yellow, and the box encloses the entire indoor space. A fine grid of points, populating the indoor space indicates the field monitors (also called sinks) are not visible in this figure due to rendering limitations.

In this method, steps 1 – 6 are a one-time modeling effort. However, steps 7 – 9 are repeated for every desired RIS configuration. Figure 2 shows a screenshot from a simulation setup in CST. From an implementation perspective, a mesh is formed which breaks down the problem so that generalized solvers can be applied. The size of the mesh depends upon the fineness of features and the size of the indoor space. The solvers have the ability to automatically select the best meshing algorithm. The complexity of the simulation for any RIS configuration depends on the size of the indoor space. For example, in one test run with an RIS with 400 unit cells, there were 3.68 million meshes for $5.5 \times 5.5 \times 1\ m^3$ (30.25 m^3 volume) indoor space. However, with the same RIS, the total number of meshes exceeded 12 million as the size for the indoor space was increased to $10 \times 10 \times 1\ m^3$ (100 m^3 volume).

Overall, the FWS-E2E method is highly accurate and can be used to simulate any type of source, unit cell, RIS, and indoor space. However, the computational complexity increases with the indoor space size. Moreover, the simulations are also repeated for every new RIS configuration.

B. HYB1-E2E MODELING

In this subsection, we briefly provide an overview of the HYB1-E2E modeling approach for computing the received powers in an RIS-assisted IPS design. The complete details of the underlying expressions to compute the channel response matrices using circuit and antenna theory are given in [22], [30], and [31]. This approach models various wireless links (AP-X, AP-RIS, RIS-X) as distance-dependent mutual impedances. The unit cell response, mutual coupling among unit cells, and RIS configurations are also modeled as appropriate impedances. Let Y_i denote the E2E channel transfer matrix at a grid point X_i in the considered indoor space. The location coordinates of X_i are (x_i, y_i, z_i). This transfer function can be obtained by modeling the direct channel and the RIS-assisted channel with impedances $\mathcal{Z}_i^{AX}$ (AP-X link) and $\mathcal{Z}_i^{ARX}$ (AP-RIS-X link). The impedance $\mathcal{Z}_i^{ARX}$ is represented as

$$\mathcal{Z}_i^{ARX} = \mathbf{z}_i^{RX} \left(\mathbf{Z}^{fix} + \mathbf{Z}^{tun} \right)^{-1} \mathbf{z}^{AR}, \tag{1}$$

where $\mathbf{z}_i^{RX} = [\mathcal{Z}_i^{RX}(1), \ldots, \mathcal{Z}_i^{RX}(N)] \in \mathcal{C}^{1\times N}$ is the impedance vector between the grid point X_i and the unit cells of the RIS, $\mathbf{z}^{AR} = [\mathcal{Z}^{AR}(1), \ldots, \mathcal{Z}^{AR}(N)]^T \in \mathcal{C}^{N\times 1}$ is the impedance vector between the AP and the unit cells of the RIS, $\mathbf{Z}^{fix} \in \mathcal{C}^{N\times N}$ is the matrix of self and mutual impedances between the pairs of unit cells, $\mathbf{Z}^{tun} = \text{diag}\left(\mathcal{Z}^{tun}(1), \ldots, \mathcal{Z}^{tun}(N)\right) \in \mathcal{C}^{N\times N}$ is a diagonal matrix containing the tunable impedances of the RIS unit cells and $[x]^T$ denotes the transpose of vector x. The vectors $\mathbf{z}_i^{RX}$ and $\mathbf{z}^{AR}$ characterize the propagation of EM waves. The variable $\mathcal{Z}^{AR}(n)$ is the impedance between the AP and the n-th unit cell of the RIS, $\mathcal{Z}_i^{RX}(n)$ is the mutual impedance between the n-th unit cell of the RIS and the grid point X_i, and $\mathcal{Z}^{tun}(n)$ is the tunable impedance of the n-th unit cell. The vector $\mathbf{z}^{AR}$ and the matrix $\mathbf{Z}^{fix}$ are computed only once as they remain the same for every grid point. Moreover, $\mathbf{Z}^{fix}$ reduces to a diagonal matrix if there is no mutual coupling between the RIS elements. The values of $\mathbf{Z}^{tun}$ are adjusted according to the states of the control elements on the unit cells to load a new RIS configuration. A big advantage of this model is considering the mutual coupling among the unit cells.

The E2E channel transfer matrix $Y_i(\mathcal{Z}^{tun}(n))$ (highlighting the dependence on the RIS configuration) is then written as

$$Y_i(\mathcal{Z}^{tun}(n)) = \mathcal{Y}_0\left(\sqrt{L_i^{AX}}\mathcal{Z}_i^{AX} - \sqrt{L_i^{ARX}}\mathcal{Z}_i^{ARX}(\mathcal{Z}^{tun}(n))\right), \quad (2)$$

where $\mathcal{Y}_0$ is the so-called mismatch line loss. We have only one AP, and we assume only one receive antenna, so this constant simplifies to $1/(4z_t)$, where z_t is the impedance of the AP antenna (typical values of z_t are between 50 to 100 Ω) [30]. It is important to highlight that in the direct link channel transfer response, we have also modeled the impact of additional losses through the term L_i^{AX}, where $0 \le L_i^{AX} \le 1$. In a similar way, in the indirect link channel transfer response, we have included an additional loss term L_i^{ARX}, where $0 \le L_i^{ARX} \le 1$. These loss terms are important because of the presence of scattering from various objects in the indoor environment, and their values depend on the nature of the obstacles between the AP or RIS and various grid points. For example, when the direct link from the AP to grid point i is completely blocked, the value of $L_i^{AX} = 0$ so that no power is received from the direct link. On the other hand, when there is no blocking object between the AP and grid point i, the value of L_i^{AX} is equal to 1. The additional losses can be adjusted depending on the objects and their locations in the indoor space. Assuming P_A as the power transmitted by the WiFi router, the received power for a given RIS configuration at a grid point X_i is computed as

$$P_i^{\text{HYB1}}(\mathcal{Z}^{tun}(n)) = P_A\left|Y_i(\mathcal{Z}^{tun}(n))\right|^2, \quad (3)$$

where $|.|$ denotes the magnitude of a complex number.

In this model, the matrix $\mathbf{Z}^{fix}$ is obtained from a full-wave simulator. However, the received power for a given location and RIS configuration is computed with the help of (3). The key steps of HYB1-E2E are described as follows:

1) Unit cell modeling: We design the unit cell in a full-wave simulator as discussed in step 2 of the FWS-E2E method.
2) RIS and mutual coupling computation: Using the unit cell designed in step 1, we create an RIS in a full-wave simulator by arranging the unit cells at the desired inter-cell spacing in a rectangular array to determine $\mathbf{Z}^{fix}$. This is a one-time computation effort for a given unit cell, RIS size and inter-cell spacing.
3) RIS configuration selection: We select an RIS configuration for which the received powers are required to be computed.
4) Received power computation: At all the grid points, we use (3) with $\mathbf{Z}^{fix}$ determined in step 2. Then, we store the received power values in a fingerprinting database.

This model is referred to as a hybrid model because we use a full-wave simulator to determine $\mathbf{Z}^{fix}$. When the inter-cell spacing is less than $\lambda/2$, the off-diagonal entries of $\mathbf{Z}^{fix}$ are non-zero. Unlike the FWS-E2E method, the complexity of computing the received powers does not increase exponentially with the indoor space size.

C. HYB2-E2E MODELING

Path loss models for RIS-assisted communication systems are available in the literature. Using the model developed in [32], the received power at a grid point X_i from the AP-RIS-X link is given as

$$P_i^{ARX} = \frac{L_i^{ARX}P_A G_A G_X A_u^2}{16\pi^2} \times \left|\sum_{n=1}^{N}\frac{\sqrt{F_i^{com}(n)}\,\gamma(n)}{D^{AR}(n)D_i^{RX}(n)}e^{\frac{-j2\pi\left(D^{AR}(n)+D_i^{RX}(n)\right)}{\lambda}}\right|^2. \quad (4)$$

In this equation, $0 \le L_i^{ARX} \le 1$ represents the additional losses on the indirect link, P_A is the transmitted power from the AP, G_A is the gain of the AP antenna, G_X is the gain of the receive antenna at grid point X_i, A_u is the area of the unit cell, $\gamma(n) = |\gamma(n)|e^{j\angle\gamma^\circ(n)}$ is the reflection coefficient of the n-th unit cell that is adjusted to obtain different RIS configurations, $D^{AR}(n)$ is the distance between the AP and the n-th unit cell, $D_i^{RX}(n)$ is the distance between the n-th unit cell and the grid point X_i, and $F_i^{com}(n)$ is the combined normalized radiation pattern. $F_i^{com}(n)$ is the product of four radiation responses

$$F_i^{com}(n) = F^A\left(\theta^A(n), \varphi^A(n)\right) \times F\left(\theta^{AR}(n), \varphi^{AR}(n)\right) \times F\left(\theta_i^{RX}(n), \varphi_i^{RX}(n)\right) \times F^X\left(\theta_i^X(n), \varphi_i^X(n)\right), \quad (5)$$

where, $F^A(.)$ is the normalized radiation pattern of the AP antenna, $F^X(.)$ is the normalized radiation pattern of the receive antenna, $F(.)$ is the normalized radiation pattern of

the unit cell, $\theta^A(n)$ and $\varphi^A(n)$ are the elevation and the azimuth angles from the AP antenna to the n-th unit cell, $\theta_i^X(n)$ and $\varphi_i^X(n)$ are the elevation and the azimuth angles from the receiver at grid point X_i to the n-th unit cell, $\theta^{AR}(n)$ and $\varphi^{AR}(n)$ are the elevation and the azimuth angles from the n-th unit cell to the AP, and $\theta_i^{RX}(n)$ and $\varphi_i^{RX}(n)$ are the elevation and the azimuth angles from the n-th unit cell to the receiver at grid point X_i. All the angles and distances between the AP and the unit cells are computed only once. However, the angles and distances between the unit cells and the receiver change when a different grid point X_i is considered.

Similarly, the received power on the direct link between the AP and the grid point X_i is also computed using the Friis equation

$$P_i^{AX} = \frac{L_i^{AX} P_A G_A G_X}{4\pi^2 \left(D_i^{AX}\right)^2} F^A\left(\theta_i^{AX}, \varphi_i^{AX}\right) F^X\left(\theta_i^{XA}, \varphi_i^{XA}\right), \quad (6)$$

where $0 \leq L_i^{AX} \leq 1$ represents the additional losses on the direct link, D_i^{AX} is the distance between the AP and the grid point X_i, θ_i^{AX} and φ_i^{AX} are the elevation and the azimuth angles between the AP and the grid point X_i, while θ_i^{XA} and φ_i^{XA} are the elevation and the azimuth angles between the grid point X_i and the AP.

The total received power at grid point X_i is the sum of the powers from the direct and the indirect paths

$$P_i^{\text{HYB2}}(\gamma(n)) = P_i^{AX} + P_i^{ARX}(\gamma(n)). \quad (7)$$

In (7) we have also made the dependence on the RIS configuration explicit by making the received power at grid point X_i a function of the reflection coefficients $\gamma(n)$ of the unit cells. Based on (7), we propose an HYB2-E2E model that utilizes some steps from the FWS-E2E model in order to improve the overall accuracy of computing the received power. The key steps of the HYB2-E2E model are the following:

1) WiFi router modeling: We model the WiFi router in a full-wave simulator as discussed in step 1 of the FWS-E2E method to obtain the normalized radiation $F^X(.)$ at all the elevation and azimuth angles.
2) Unit cell: We design the unit cell in a full-wave simulator as discussed in step 2 of the FWS-E2E method and determine the normalized radiation response $F(.)$ at all elevation and azimuth angles.
3) Radiation response computation of receiver: IPS users generally have different types of devices. Owing to the diversity of receiving devices, it is challenging to model the radiation response of the receiver. However, we can identify some commonly used devices and simulate their normalized radiation response $F^X(.)$ in a full wave simulator. Alternatively, we can assume an isotropic receiver for simplicity and set the normalized radiation response of the receiver to 1 for all the elevation and azimuth angles.
4) RIS configuration selection: We select an RIS configuration for which the received powers is to be computed.
5) Received power computation: At all the grid points, we use (7) with the normalized radiation responses determined in steps 1 – 3 to compute the received powers and store them in a fingerprinting database.

This method uses a few steps from the FWS-E2E method to improve the accuracy. The use of a full-wave simulator to determine the normalized radiation responses is a one-time effort for a given AP and unit cell design. After these radiation responses are obtained, we compute the received powers using (7). Therefore, unlike the FWS-E2E method, the complexity of computing the received powers does not increase exponentially with the size of the indoor space.

In the literature, the normalized radiation response of a unit cell is often approximated as $F(\theta, \varphi) = \cos(\theta)$. However, this approximation results in significant errors in the received power because, in an IPS design, we are interested in the received powers at several closely spaced grid points. In Figure 3, we highlight the difference between the normalized radiation response obtained through full-wave simulations for a unit cell from the literature that uses 1 PIN diode [33] and the $\cos(\theta)$ radiation pattern. The difference between the two curves increases as the elevation angle θ goes from 0 to $\pi/2$. The maximum difference between the two radiation responses is around 35%, which can lead to significant errors in the received power and hence impact the performance of the IPS design. The difference between the two curves can never be completely eliminated but it can be reduced by adjusting the power q of a parametric $\cos^{\frac{1}{q}}(\theta)$ radiation response.

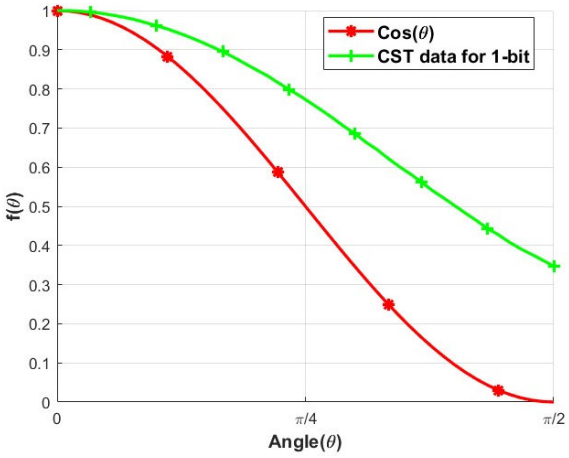

FIGURE 3. Difference between the normalized radiation response of an actual a unit cell obtained through full-wave simulations versus the cos(θ) radiation pattern.

IV. SELECTING RIS CONFIGURATIONS FOR IPS DESIGN

In an RIS-assisted IPS design, a new radio map of the indoor space is generated by changing the RIS configuration. The total number of radio maps depends on the number of unit cells on the RIS and the range in which the phases of the unit cells can be varied. A 100 unit cell RIS with two

discrete phases per unit cell has 2^{100} different configurations. Exploring such a large set of RIS configurations for an IPS design is a challenging task. In this section, we discuss some methods to identify those RIS configurations that have the potential of generating interesting radio maps for improving the performance of an IPS design.

We identify the grid points in the indoor space from where the localization requests are expected to arrive more frequently. We collect all such grid points in the set $\mathcal{X}$, where K denotes the total number of elements in this set. We determine one RIS configuration for every grid point in $\mathcal{X}$ that maximizes the received power at the particular grid point. In this way, we generate a total of K radio maps for the fingerprinting database. The i-th radio map is the one that utilizes the RIS configuration for maximizing the received power at the i-th grid point in the set $\mathcal{X}$.

Let P_i^r denote the received power at grid point i. In the HYB1-E2E model, the received power changes by adjusting the tunable impedances of the unit cells, while in HYB2-E2E, it changes by adjusting the reflection coefficients. However, in both models, the tunable impedances, as well as the reflection coefficients, are functions of the phase shifts that are imposed by the unit cells on the EM waves. Therefore, to develop a generic optimization problem for both models, let α_n denote the phase shift of the n-th unit cell so that the received power is represented as $P_i^r(\alpha_n)$. The values of α_n are either continuous or discrete depending on the unit cells used in the RIS design. Therefore, we have two types of optimization problems:

$$\text{P1}: \max_{\alpha_n} \; P_i^r(\alpha_n) \tag{8}$$

$$\text{subject to: } \alpha_n \in [\alpha_{\min}, \alpha_{\max}], \quad \forall n \tag{9}$$

where, $\alpha_{\min} \geq 0$ and $\alpha_{\min} < \alpha_{\max} < 2\pi$. In P1, the optimization variables can vary in a continuous range. Therefore, it is a continuous optimization problem. Similarly, we have a discrete optimization problem P2 as follows:

$$\text{P2}: \max_{\alpha_n} \; P_i^r(\alpha_n) \tag{10}$$

$$\text{subject to: } \alpha_n \in \{\tilde{\alpha}_1, \ldots, \tilde{\alpha}_L\}, \quad \forall n \tag{11}$$

where, $\tilde{\alpha}_l, \; \forall l$ are the L discrete phase shifts. The minimum number of discrete phase shifts in P2 is 2 ($L = 2$) for unit cells that employ a single PIN diode.

The optimal solution of P1 is determined by taking the partial derivatives of $P_i^r(\alpha_n)$ w.r.t. α_n. On the other hand, P2 is more difficult to solve because of the discrete nature of the optimization variables. For the received power equation in the HYB1-E2E model (3), iterative and analytical solutions for P1 can be found in [34]. The algorithm directly optimizes the values of $\mathcal{Z}^{tun}(n), \; \forall n$. An iterative solution for P1 based on the gradient update rule is developed next using the total power in (7) for the HYB2-E2E model. The optimization variables (α_n) are only in the indirect link power in (4), which is rewritten as

$$P_i^{ARX} = B \left| \sum_{n=1}^{N} C_i(n) e^{j\alpha_n} \right|^2, \tag{12}$$

where, $B_i = \frac{L_i^{ARX} P_A G_A G_X A_u^2}{16\pi^2}$ and

$$C_i(n) = \frac{\sqrt{F_i^{com}(n)}\,|\gamma(n)|}{D^{AR}(n) D_i^{RX}(n)} e^{\frac{-j2\pi\left(D^{AR}(n)+D_i^{RX}(n)\right)}{\lambda}}.$$

The partial derivative of the total power is obtained as

$$\frac{\partial P_i^r(\alpha_n)}{\partial \alpha_n} = 2B_i \times \text{Im}\left(|C_i(n)|^2 + \sum_{m=1, m\neq n}^{N} C_i^*(n) C_i(m) e^{j(\alpha_m - \alpha_n)} \right), \; \forall n. \tag{13}$$

Using these partial derivatives, we develop the following iterative algorithm.

1) Randomly initialize all the phases between $\alpha_{\min}$ and $\alpha_{\max}$.
2) Compute all the partial derivatives according to (13).
3) Normalize the partial derivatives:
$$\frac{\partial P_i^r(\alpha_n)}{\partial \alpha_n} \leftarrow \frac{1}{\rho} . \frac{\partial P_i^r(\alpha_n)}{\partial \alpha_n}, \quad \forall n$$
where, $\rho = \max_n \left(\frac{\partial P_i^r(\alpha_n)}{\partial \alpha_n} \right)$.
4) Update all the phases using the gradient update rule:
$$\alpha_n \leftarrow \alpha_n + \eta \frac{\partial P_i^r(\alpha_n)}{\partial \alpha_n}, \quad \forall n$$
where η is the learning rate or the step size.
5) Calculate the objective function and repeat steps 2 and 3 until the increment in the received power is less than some preset threshold or the number of iterations reaches the maximum value.

This algorithm converges to a locally optimal solution and returns the phases of the unit cells.

Finding the optimal solution of P2 with discrete optimization variables is more challenging. For this problem, we use a non-convex optimization technique with the ability to handle discrete variables such as a Genetic Algorithm (GA), which provides a sub-optimal solution [35]. We model the problem so that the GA chromosomes are the predicted values of the discrete optimization variables. We set a target value for the received power at the desired grid point i and then use a fitness function that minimizes the mean-squared error between the target value and the received power value from the RIS configuration in each iteration. Typically, the received power value is high when the phases are continuously adjusted. Therefore, the received power obtained from the corresponding P1 optimization problem can also be used as a target value in the GA fitness function. According to the operation of a GA controlled through its hyperparameters, various RIS configurations are tested until

there is no further reduction in the fitness function or the number of iterations reaches the maximum. GA can be used with the received power expressions of both HYB1-E2E and HYB2-E2E models.

V. SIMULATION RESULTS

We consider a $10 \times 10 \times 3\ m^3$ room. In the local coordinate system, the x-coordinate spans the width, the y-coordinate spans the height, and the z-coordinate spans the length of the room. A square 40×40 unit cell RIS (1600 elements) with $\lambda/2$ inter-cell spacing is assumed to be placed in the x-y plane at the center of the wall. Moreover, the center of the RIS is assumed to be the origin of the considered local coordinate system. Only one WiFi router operating at 5.2 GHz is in the room, and its location coordinates are $(5, 3, 5)$. The transmit power of the WiFi router is 1 W, and for simplicity, we assume an omnidirectional antenna. To develop a fingerprinting database for an IPS, the entire room is divided into a grid with a uniform spacing of 0.5 m in each dimension. The received power values, unless otherwise specified, are always computed at the grid points located on an receiver plane whose center lies at a distance of z_r from the origin. This plane has a total of 147 grid points. We assume $L_i^{AX} = 0,\ \forall i$ (no direct link) and $L_i^{ARX} = 1,\ \forall i$ (no additional losses on the indirect link). We also assume that the receiver does not utilize directive antennas.

For the continuous case, in both the hybrid models, we assume that the phases of all the unit cells on the RIS are continuously varied between $[0, 2\pi)$. As for HYB1-E2E, the values of various parameters are taken from [34]. As for HYB2-E2E, we assume that the normalized radiation response of the unit cell is $\cos^{\frac{1}{3}}(\theta)$, where θ represents the elevation angle, while the variations due to the changes in the azimuth angle are assumed to be negligible. For the discrete case, we use a 1-bit unit design proposed in [33]. The unit cell produces a 180° phase difference between the two diode states. The PIN diode is modeled using the lumped element method, and its impedance in the ON and OFF state is computed as $0.8 + j22.87$ and $-64.57j$, respectively. A 40×40 unit cell RIS is designed in CST to compute the self and mutual coupling effects, which are collected in $\mathbf{Z}^{fix}$. The mutual coupling is strong among the neighboring unit cells, which results in a sparse matrix with the off-diagonal entries approaching zero as we move away from the diagonal elements in either direction. Similarly, we obtain the normalized radiation response denoted as $F_i^{com}(n)$ for HYB2-E2E by using CST. This simulation begins by emitting a signal from the WiFi router located inside the room, which then interacts with the RIS. A controller adjusts the phases of the RIS unit cells to generate the best configuration for maximizing the signal reception at the target point based on the considered models. We find the best RIS configuration that maximizes the received power at the $(5, 1.5, 5)$ grid point from where we expect to receive a higher number of localization requests. In Figure 4, we plot the heat maps of the normalized powers (dB) in the receiver plane at $z_r = 5$ for HYB1-E2E and HYB2-E2E, respectively. The target grid point $(5, 1.5, 5)$ is shown at the bottom right corner of the plane. In both cases, the algorithms clearly maximize the received power at the target location. The received powers at all the other grid points on the plane are then computed using the tunable impedance values and RIS configuration that maximizes the received power at the target location. These computations are made with the analytical equations and saved in the fingerprinting database along with other relevant metadata. For the discrete case, we use the GA function in MATLAB with default parameters. The target grid point is the same, i.e., $(5, 1.5, 5)$. In the considered case study, the GA terminates and manages to find a good quality solution for HYB1-E2E and HYB2-E2E. Using the RIS configuration (diode ON/OFF states on each unit cell) obtained from the GA, we compute the received power at all the grid points on a plane located at $z_r = 5$ m from the RIS center. We normalize the powers and plot them as heat maps in Figures. 4c and 4d. In all the heat maps presented in Figure 4, the RSS is the strongest at the target grid point. The proposed algorithms are able to concentrate a large amount of power at the desired grid point.

In order to quantify the ability of various algorithms to concentrate power at the desired grid point, we define a metric called power ratio (PR). The PR is defined as the percentage (%) of total power in the receiving plane that is directed at the target grid point, i.e.,

$$\text{PR} = \frac{P_{\text{tar}}}{P_{\text{sum}}} \times 100$$

where P_{tar} is the power at the target point and P_{sum} is the total power in the receiving plane. For the heat maps shown in Figure 4 the PRs in the continuous case for HYB1-E2E and HYB2-E2E are 79.59% and 85.66% respectively. On the other hand, in the discrete case, the PRs for HYB1-E2E and HYB2-E2E are 23.71% and 40.02% respectively. The PR for the discrete cases may be further improved by using unit cells that provide more discrete states.

VI. EXPERIMENTAL RESULTS & COMPLEXITY COMPARISON

A. EXPERIMENTAL RESULTS

In this section, we present some experimental results. These results are obtained with the help of a manufactured 1-bit (discrete) RIS. The RIS consists of a total of 756 unit cells arranged in a 28×27 rectangular arrangement. Further details about the RIS can be found in [36]. We carried out the experiments in the Microwave laboratory at Lahore University, Pakistan. The dimensions of the experimental area are $3 \times 2 \times 2\ m^3$. The complete setup consisting of two universal software radio peripherals (USRPs), two identical horn antennas operating at 5.2 GHz (one as a transmitter and the other as a receiver) and the two computers is shown in Figure 5. The origin of the local coordinate system is assumed to be the center of the RIS. In this coordinate system, the

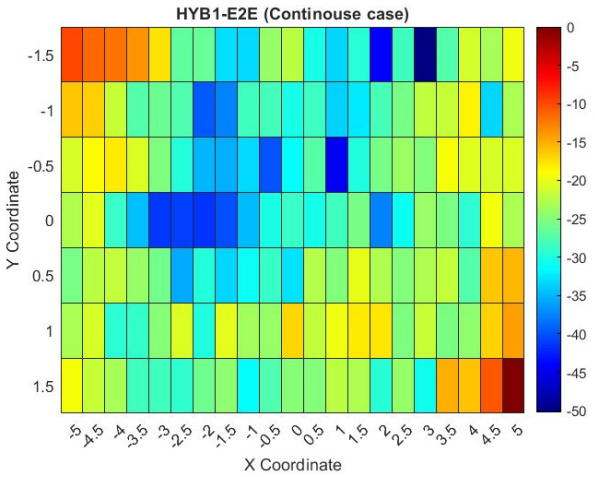

(a) **HYB1-E2E Model: Received power heat map for the continuous optimization problem**

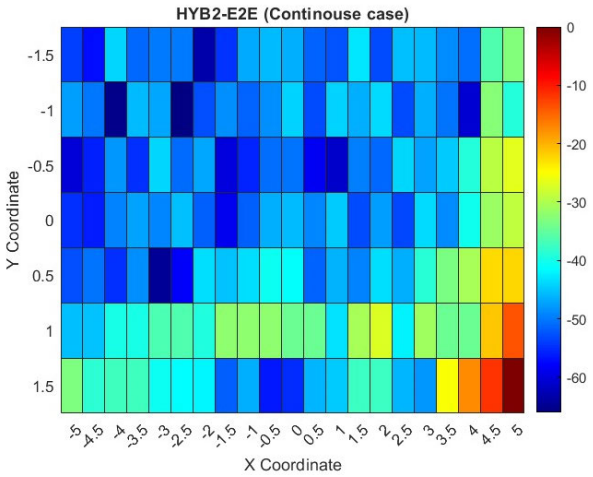

(b) **HYB2-E2E Model: Received power heat map for the continuous optimization problem**

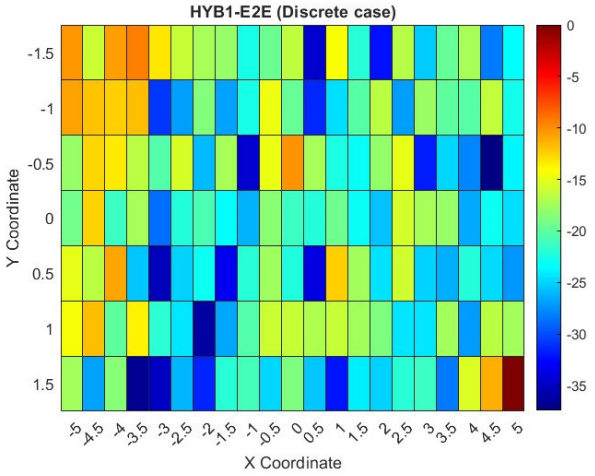

(c) **HYB1-E2E Model: Received power heat map for the discrete optimization problem (in CST, a 1-bit unit cell, [35], exhibits a self-impedance of 75.367 and a mutual impedance of around 1.309 with neighboring cells.)**

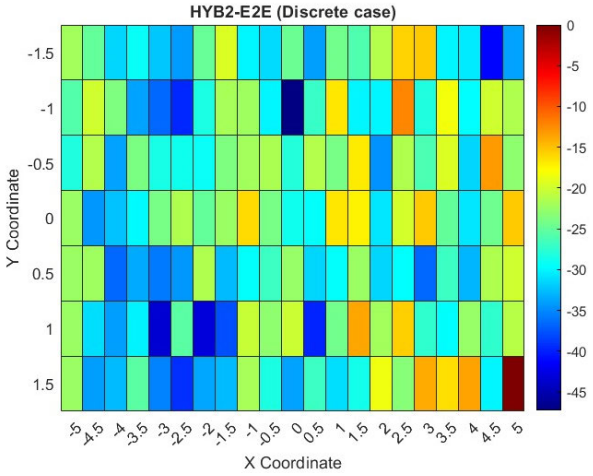

(d) **HYB2-E2E Model: Received power heat map for the discrete optimization problem**

FIGURE 4. Received power in an x-y plane at $z_r = 5$ m from RIS center. The target grid point is (5, 1.5, 5), located in the bottom right corner where the power is maximized.

transmitter (Tx) is located at $(-1, 0, 0.5)$. It should be noted that there are also some additional power losses in various cables and measurement equipment. These losses are determined to be 29.76 *dB* using the calibration method described in [32].

The target grid point where we intend to maximize the power is located at $(1.5, 0, 2)$. At this point, we place the Rx horn antenna. For HYB1-E2E and HYB2-E2E, we run the GA and obtain the RIS configurations that maximize the power at the target grid point. Using these configurations we also compute the power values at multiple grid points with the help of the considered hybrid models, and then add the losses in the simulated values. We then load the RIS configuration obtained from HYB1-E2E in the RIS controller and experimentally measure the actual power value at the target grid point. The USRPs serve as the hardware interface for both transmitting and receiving radio signals. The transmitter USRP generates a radio signal that is then emitted through its connected horn antenna, operating at a frequency of 5.2 *GHz*. The emitted signal interacts with the RIS, which is strategically positioned within the environment. The RIS, controlled via a controller, is configured to manipulate the phase and hence the direction of the incoming signal to optimize its path towards the receiver. This optimization is based on the RIS configurations determined by the GA, aiming to maximize the signal reception at the target grid point. Once the signal is reflected and manipulated by the RIS, it is captured by the receiver horn antenna placed at the specified grid point. The receiver USRP, connected to this antenna, then processes the received signal to measure its power. By manually moving the Rx antenna and measuring the power at multiple grid points, we explore

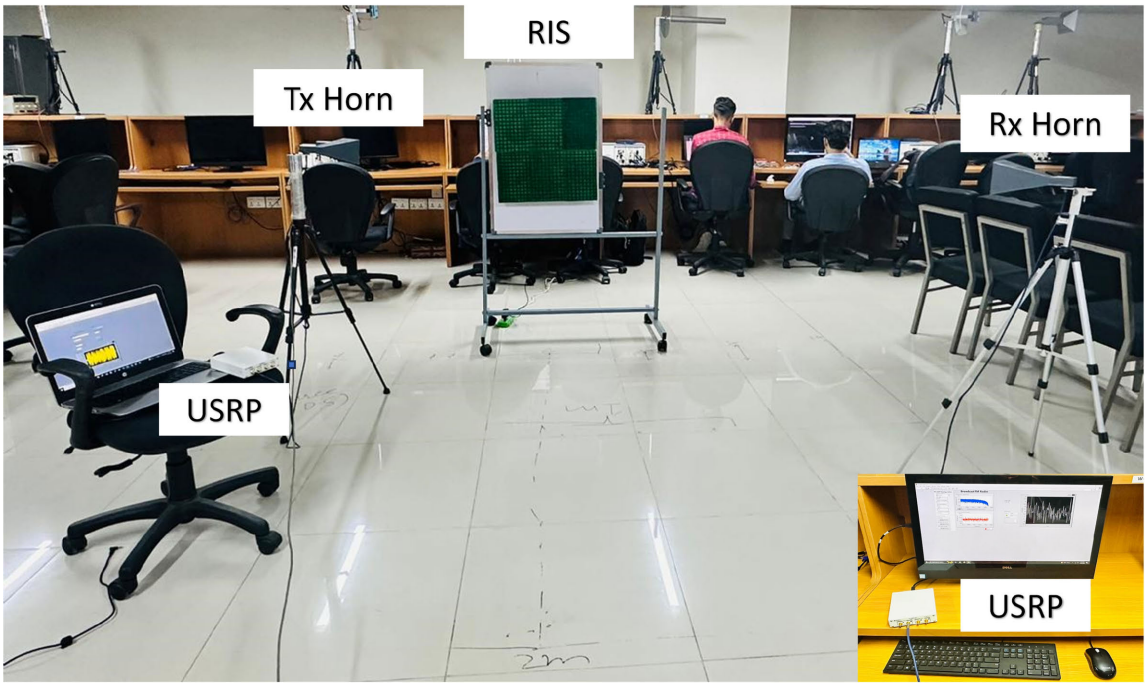

FIGURE 5. Experimental setup. We have a 28 × 27 rectangular RIS, two horn antennas at 5.2 GHz, two USRPs and two computers. The experimental area is 3 × 2x2 m^3.

the spatial effectiveness of the optimized RIS configurations. After completing the measurements with the configuration from HYB1-E2E, we switch to the configuration obtained from HYB2-E2E and repeat the measurement process. This procedure yields two sets of experimental measurements and two sets of simulated measurements for each considered hybrid model, providing a comprehensive dataset to evaluate the performance of RIS-assisted signal enhancement in the considered experimental setup.

The measured and simulated RSS values are plotted in Figure 6. In these figures, we have not normalized the RSS values. We observe that the optimized RIS configurations are different for the two considered models, therefore the RSS values are also different. However, in both cases, the algorithms are able to maximize the power at the target grid point. The difference between the simulated and the experimental values is also small. The PR obtained at the target grid point is more than 50% even in the experimental results for both hybrid models. Interestingly, the RSS values at all the other grid points are almost 8 to 10 *dB* lower than the RSS value at the target grid point, which facilitates localization. Therefore, we can easily generate a set of RIS configurations with the proposed algorithms and then use the hybrid models to create the radio maps and quickly develop a fingerprinting database.

B. COMPLEXITY COMPARISON

These experiments are also helpful in quantifying the complexity of an RF measurement campaign for developing a fingerprinting database for an RIS-assisted IPS. In the considered experiments, we took the actual measurements at the grid points for a given RIS configuration. For these measurements, we first adjusted the RIS configuration through an RIS controller and then measured the received power at each grid point. In the generic case, if we assume that β minutes are required to measure the power with a physical device at one grid point, then $L\beta$ minutes are needed to cover a region (plane or room) divided into L grid points. We repeat the process for K RIS configurations. Therefore, assuming the time to switch an RIS configuration is negligible, we still require $LK\beta$ minutes for manual site surveying. In our experiments, it took 5 minutes to record the RSS from one grid point and then accurately move on to the next grid point. Therefore, in a plane with $L = 147$ and $\beta = 5$, the total time becomes 735 minutes or 12.25 hours. Assuming 147 RIS configurations (one per grid point), the time complexity becomes 1800 hours which is equal to 75 days.

The FWS-E2E modeling approach is also time consuming and computational-intensive. In Figure 7 we present the total time and total meshes estimated by CST to determine the received power for different room volumes (m^3) on a Core i5 laptop. In these simulations, we assumed an RIS with 16 unit cells. The estimated time to complete the simulations increased from millions of hours to billions of hours as we increased the room volume from 0.07 m^3 to 300 m^3. Generally, full-wave simulations are performed on server machines with huge computing power that reduces the

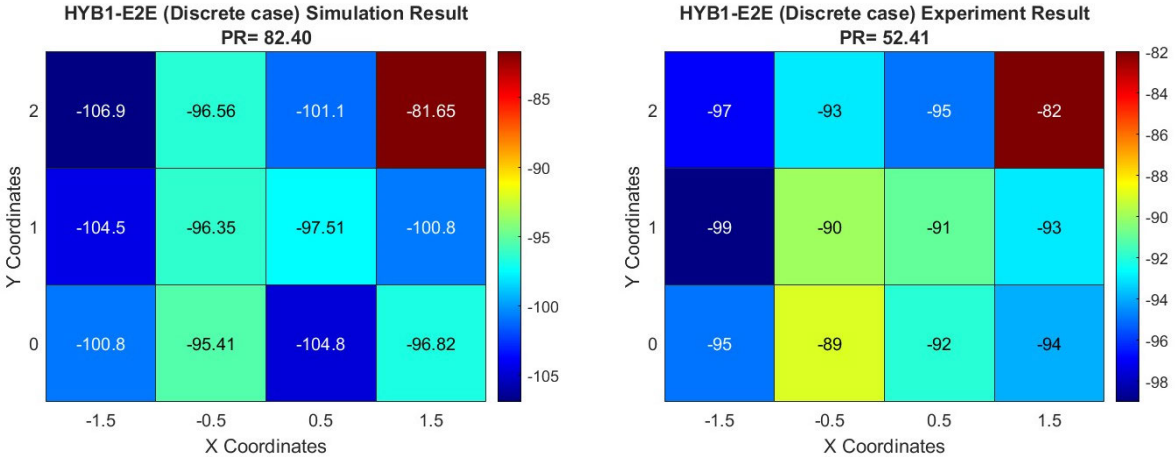

(a) HYB1-E2E Model (discrete case): Simulation results.

(b) HYB1-E2E Model (discrete case): Experimental results.

(c) HYB2-E2E Model (discrete case): Simulation results.

(d) HYB2-E2E Model (discrete case): Experimental results.

FIGURE 6. Received power heat maps obtained from simulations and hardware experiments for the two hybrid models according to the layout of the experimental setup. The target grid point is (1.5, 0, 2).

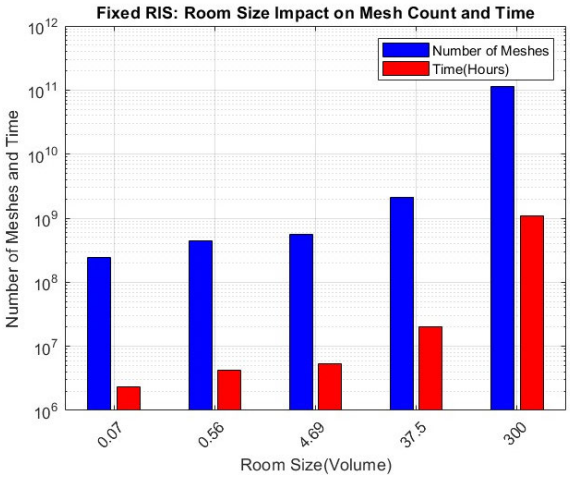

FIGURE 7. Complexity of the FWS-E2E model. The number of meshes and simulation time in hours estimated by the CST on a Core i5 laptop for different room volumes.

simulation time to few weeks. It is obvious that despite being computational-intensive, the FWS-E2E method still provides several benefits over the labor-intensive RF measurement campaign.

Finally, the complexity of obtaining the values of the received power from the hybrid models is extremely small compared to the FWS-E2E model and the RF measurement campaign. In the discrete case, the time required to find the self and mutual impedance among the unit cells in CST for the 1-bit discrete RIS is approximately 150 hours on a dual Intel Xeon gold 6240 processor. However, it is a one-time computational effort for a given RIS and does not change with the RIS configurations. On the other hand, it took us less than 10 minutes to find the radiation response of the unit cell in CST. Once we have the required CST data, we first run the chosen algorithm after fixing a target grid point and then determine the RIS configuration. After finding the RIS configuration, the power at all the grid points in the plane can be determined in few minutes even on an ordinary core i5 machine.

We want to point out that the RIS configuration obtained form the simulations is also required for manual the site surveying and FWS-E2E approaches. Therefore, the time

required to find the best RIS configurations is the same in all the cases. However, the hybrid models drastically reduce the effort required for computing the power values in the indoor space. The complexity of the hybrid methods also scales favorably with the increase in the indoor space volume. Therefore, the hybrid methods can be used to develop a fingerprinting database for an RIS-assisted IPS. Moreover, the algorithms to find the best RIS configurations reduce the total number of configurations needed to achieve high localization accuracy. Overall, this paper establishes a foundational framework for RIS-assisted IPS, focusing on optimizing the phase shifts of RIS unit cells and utilizing E2E propagation models to minimize the time and cost complexities associated with IPS. This groundwork lays the foundation for future advancements by developing effective RIS configurations for precise user localization. The localization algorithms and experimental evaluation of localization error are left as a follow-up work.

VII. CONCLUSION

In this paper, we presented fingerprinting database development methods for RIS-assisted IPS. The algorithms to determine the best RIS configurations for achieving high localization accuracy were also discussed. The proposed algorithms were able to focus a large amount of power at the desired grid point. A fingerprinting database of such RIS configurations can be developed with the help of the proposed hybrid models in an efficient and scalable manner. We also built a 28×27 unit cell RIS and used it to measure the actual RSS values for the RIS configurations obtained from the two hybrid models. We observed a small difference between the simulated and the measured RSS values for both the models. The RSS value at the target grid point was almost 10 dB higher than the rest of the grid points in the obtained experimental results. Therefore, the hybrid models and the algorithms to determine the best RIS configurations can be used for developing a fingerprinting database for RIS-assisted IPS in a scalable way.

REFERENCES

[1] N. U. Hassan, A. Naeem, M. A. Pasha, T. Jadoon, and C. Yuen, "Indoor positioning using visible LED lights: A survey," *ACM Comput. Surv.*, vol. 48, no. 2, pp. 1–32, Nov. 2015.

[2] A. Yassin, Y. Nasser, M. Awad, A. Al-Dubai, R. Liu, C. Yuen, R. Raulefs, and E. Aboutanios, "Recent advances in indoor localization: A survey on theoretical approaches and applications," *IEEE Commun. Surveys Tuts.*, vol. 19, no. 2, pp. 1327–1346, 2nd Quart., 2017.

[3] T. Lan, X. Wang, Z. Chen, J. Zhu, and S. Zhang, "Fingerprint augment based on super-resolution for WiFi fingerprint based indoor localization," *IEEE Sensors J.*, vol. 22, no. 12, pp. 12152–12162, Jun. 2022.

[4] M. Abbas, M. Elhamshary, H. Rizk, M. Torki, and M. Youssef, "WiDeep: WiFi-based accurate and robust indoor localization system using deep learning," in *Proc. IEEE Int. Conf. Pervasive Comput. Commun. (PerCom*, Mar. 2019, pp. 1–10.

[5] J. Xue, J. Liu, M. Sheng, Y. Shi, and J. Li, "A WiFi fingerprint based high-adaptability indoor localization via machine learning," *China Commun.*, vol. 17, no. 7, pp. 247–259, Jul. 2020.

[6] Z. Chen, H. Zou, J. Yang, H. Jiang, and L. Xie, "WiFi fingerprinting indoor localization using local feature-based deep LSTM," *IEEE Syst. J.*, vol. 14, no. 2, pp. 3001–3010, Jun. 2020.

[7] Q. Liang and M. Liu, "An automatic site survey approach for indoor localization using a smartphone," *IEEE Trans. Autom. Sci. Eng.*, vol. 17, no. 1, pp. 191–206, Jan. 2020.

[8] C. Huang, A. Zappone, G. C. Alexandropoulos, M. Debbah, and C. Yuen, "Reconfigurable intelligent surfaces for energy efficiency in wireless communication," *IEEE Trans. Wireless Commun.*, vol. 18, no. 8, pp. 4157–4170, Aug. 2019.

[9] M. Jian, G. C. Alexandropoulos, E. Basar, C. Huang, R. Liu, Y. Liu, and C. Yuen, "Reconfigurable intelligent surfaces for wireless communications: Overview of hardware designs, channel models, and estimation techniques," *Intell. Converged Netw.*, vol. 3, no. 1, pp. 1–32, Mar. 2022.

[10] G. C. Alexandropoulos, K. Stylianopoulos, C. Huang, C. Yuen, M. Bennis, and M. Debbah, "Pervasive machine learning for smart radio environments enabled by reconfigurable intelligent surfaces," *Proc. IEEE*, vol. 110, no. 9, pp. 1494–1525, Sep. 2022.

[11] T. Gong, I. Vinieratou, R. Ji, C. Huang, G. C. Alexandropoulos, L. Wei, Z. Zhang, M. Debbah, H. V. Poor, and C. Yuen, "Holographic MIMO communications: Theoretical foundations, enabling technologies, and future directions," *IEEE Commun. Surveys Tuts.*, 2023.

[12] A. Abrardo, A. Toccafondi, and M. Di Renzo, "Design of reconfigurable intelligent surfaces by using s-parameter multiport network theory–optimization and full-wave validation," 2023, *arXiv:2311.06648*.

[13] N. U. Hassan, J. An, M. Di Renzo, M. Debbah, and C. Yuen, "Efficient beamforming and radiation pattern control using stacked intelligent metasurfaces," *IEEE Open J. Commun. Soc.*, vol. 5, pp. 599–611, 2024.

[14] M. Di Renzo, A. Zappone, M. Debbah, M.-S. Alouini, C. Yuen, J. de Rosny, and S. Tretyakov, "Smart radio environments empowered by reconfigurable intelligent surfaces: How it works, state of research, and the road ahead," *IEEE J. Sel. Areas Commun.*, vol. 38, no. 11, pp. 2450–2525, Nov. 2020.

[15] J. Xu, C. Yuen, C. Huang, N. Ul Hassan, G. C. Alexandropoulos, M. Di Renzo, and M. Debbah, "Reconfiguring wireless environments via intelligent surfaces for 6G: Reflection, modulation, and security," *Sci. China Inf. Sci.*, vol. 66, no. 3, Mar. 2023, Art. no. 130304.

[16] T. Ma, Y. Xiao, X. Lei, W. Xiong, and Y. Ding, "Indoor localization with reconfigurable intelligent surface," *IEEE Commun. Lett.*, vol. 25, no. 1, pp. 161–165, Jan. 2021.

[17] H. Zhang, H. Zhang, B. Di, K. Bian, Z. Han, and L. Song, "MetaLocalization: Reconfigurable intelligent surface aided multi-user wireless indoor localization," *IEEE Trans. Wireless Commun.*, vol. 20, no. 12, pp. 7743–7757, Dec. 2021.

[18] H. Zhang, J. Hu, H. Zhang, B. Di, K. Bian, Z. Han, and L. Song, "MetaRadar: Indoor localization by reconfigurable metamaterials," *IEEE Trans. Mobile Comput.*, vol. 21, no. 8, pp. 2895–2908, Aug. 2022.

[19] C. Pan, G. Zhou, K. Zhi, S. Hong, T. Wu, Y. Pan, H. Ren, M. D. Renzo, A. Lee Swindlehurst, R. Zhang, and A. Y. Zhang, "An overview of signal processing techniques for RIS/IRS-aided wireless systems," *IEEE J. Sel. Topics Signal Process.*, vol. 16, no. 5, pp. 883–917, Aug. 2022.

[20] T. Wu, C. Pan, Y. Pan, H. Ren, M. Elkashlan, and C.-X. Wang, "Fingerprint based mmWave positioning system aided by reconfigurable intelligent surface," *IEEE Wireless Commun. Lett.*, 2023.

[21] E. C. Strinati, G. C. Alexandropoulos, V. Sciancalepore, M. Di Renzo, H. Wymeersch, D.-T. Phan-Huy, M. Crozzoli, R. D'Errico, E. De Carvalho, P. Popovski, P. Di Lorenzo, L. Bastianelli, M. Belouar, J. E. Mascolo, G. Gradoni, S. Phang, G. Lerosey, and B. Denis, "Wireless environment as a service enabled by reconfigurable intelligent surfaces: The RISE-6G perspective," in *Proc. Joint Eur. Conf. Netw. Commun. 6G Summit (EuCNC/6G Summit)*, Jun. 2021, pp. 562–567.

[22] G. Gradoni and M. Di Renzo, "End-to-end mutual coupling aware communication model for reconfigurable intelligent surfaces: An electromagnetic-compliant approach based on mutual impedances," *IEEE Wireless Commun. Lett.*, vol. 10, no. 5, pp. 938–942, May 2021.

[23] S. W. Ellingson, "Path loss in reconfigurable intelligent surface-enabled channels," in *Proc. IEEE 32nd Annu. Int. Symp. Pers., Indoor Mobile Radio Commun. (PIMRC)*, Sep. 2021, pp. 829–835.

[24] L. Alsmadi, X. Kong, K. Sandrasegaran, and G. Fang, "An improved indoor positioning accuracy using filtered RSSI and beacon weight," *IEEE Sensors J.*, vol. 21, no. 16, pp. 18205–18213, Aug. 2021.

[25] L. Dai, B. Wang, M. Wang, X. Yang, J. Tan, S. Bi, S. Xu, F. Yang, Z. Chen, M. Di Renzo, C.-B. Chae, and L. Hanzo, "Reconfigurable intelligent surface-based wireless communications: Antenna design, prototyping, and experimental results," *IEEE Access*, vol. 8, pp. 45913–45923, 2020.

[26] N. Virushabadoss, B. Shamsundar, R. Henderson, and A. Nosratinia, "EM modeling considerations on reconfigurable intelligent surfaces for system design," in *Proc. IEEE Microw., Antennas, Propag. Conf. (MAPCON)*, Dec. 2022, pp. 1382–1387.
[27] M. Dunna, C. Zhang, D. Sievenpiper, and D. Bharadia, "ScatterMIMO: Enabling virtual MIMO with smart surfaces," in *Proc. 26th Annu. Int. Conf. Mobile Comput. Netw.*, Apr. 2020, pp. 1–14.
[28] M. Rossanese, P. Mursia, A. Garcia-Saavedra, V. Sciancalepore, A. Asadi, and X. Costa-Perez, "Designing, building, and characterizing RF switch-based reconfigurable intelligent surfaces," in *Proc. 28th Annu. Int. Conf. Mobile Comput. Netw.*, Oct. 2022, pp. 69–76.
[29] W. Tang, M. Z. Chen, X. Chen, J. Y. Dai, Y. Han, M. Di Renzo, Y. Zeng, S. Jin, Q. Cheng, and T. J. Cui, "Wireless communications with reconfigurable intelligent surface: Path loss modeling and experimental measurement," *IEEE Trans. Wireless Commun.*, vol. 20, no. 1, pp. 421–439, Jan. 2021.
[30] M. Di Renzo, F. H. Danufane, and S. Tretyakov, "Communication models for reconfigurable intelligent surfaces: From surface electromagnetics to wireless networks optimization," *Proc. IEEE*, vol. 110, no. 9, pp. 1164–1209, Sep. 2022.
[31] P. Mursia, T. Mazloum, F. Munoz, V. Sciancalepore, G. Gradoni, R. D Errico, M. Di Renzo, X. Costa-Perez, A. Clemente, and G. Lerosey, "Empirical validation of the impedance-based RIS channel model in an indoor scattering environment," 2023, *arXiv:2311.12628*.
[32] W. Tang, X. Chen, M. Z. Chen, J. Y. Dai, Y. Han, M. Di Renzo, S. Jin, Q. Cheng, and T. J. Cui, "Path loss modeling and measurements for reconfigurable intelligent surfaces in the millimeter-wave frequency band," *IEEE Trans. Commun.*, vol. 70, no. 9, pp. 6259–6276, Sep. 2022.
[33] H. Yang, X. Cao, F. Yang, J. Gao, S. Xu, M. Li, X. Chen, Y. Zhao, Y. Zheng, and S. Li, "A programmable metasurface with dynamic polarization, scattering and focusing control," *Sci. Rep.*, vol. 6, no. 1, p. 35692, Oct. 2016.
[34] X. Qian and M. Di Renzo, "Mutual coupling and unit cell aware optimization for reconfigurable intelligent surfaces," *IEEE Wireless Commun. Lett.*, vol. 10, no. 6, pp. 1183–1187, Jun. 2021.
[35] A. Rafique, N. U. Hassan, M. Zubair, I. H. Naqvi, M. Q. Mehmood, M. Di Renzo, M. Debbah, and C. Yuen, "Reconfigurable intelligent surfaces: Interplay of unit-cell-and surface-level design and performance under quantifiable benchmarks," *IEEE Open J. Commun. Soc.*, 2023.
[36] F. Ramzan, A. Rafique, D. Khan, N. U. Hassan, I. H. Naqvi, M. Q. Mehmood, M. Zubair, and Y. Massoud, "Reconfigurable intelligent surfaces: Field trial campaign for performance evaluation from near-to far-field regions," in *Proc. IEEE Int. Symp. Circuits Syst. (ISCAS)*, May 2023, pp. 1–4.

AISHA JAVED received the B.S. degree in electrical engineering from the University of Engineering and Technology (UET), Lahore, Pakistan, in 2016, and the M.S. degree from the Electrical Engineering Program, National University of Sciences and Technology (NUST), Islamabad, Pakistan, in 2019. Her master's thesis was on "Optimization of Access Points Deployment for Enhancing Indoor Localization in a WiFi Environment." In 2019, she joined the Ph.D. Program with Lahore University of Management Sciences (LUMS), Lahore, as a full-time Ph.D. Graduate Fellow. At the Communication Laboratory, she has been working on indoor localization and reconfigurable intelligent surfaces (RIS) with the help of MATLAB and various EM simulation tools. Her research interests include wireless communication systems, indoor positioning systems, and computer networks.

NAVEED UL HASSAN (Senior Member, IEEE) received the B.E. degree from the College of Aeronautical Engineering, Risalpur, Pakistan, in 2002, and the M.S. and Ph.D. degrees from Ecole Superieure d Electricite, Gif-sur-Yvette, France, in 2006 and 2010, respectively. He is an Associate Professor of electrical engineering with Lahore University of Management Sciences (LUMS), Pakistan. He has completed several impactful research projects and published over 100 research papers at international journals and conferences. His research interests include wireless communication, smart energy systems, blockchain technology, and indoor positioning systems. He serves as an Associate Editor for *Springer Nature Computer Science* and *IET Smart Grid*.

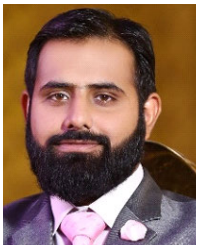

AMMAR RAFIQUE received the B.S. degree in electrical engineering from UET, Lahore, in 2015, and the M.S. degree from the Electrical Engineering Program, NUCES Lahore, in 2018. His master's thesis was on machine learning-based automated fault diagnosis of synchronous machines, which heavily relied on EM simulation tools. In 2018, he joined as a Visiting Faculty Laboratory Instructor with NUCES Lahore, which he continued for a year. In 2019, he joined the Ph.D. Program with ITU, Lahore, as a full-time Ph.D. Graduate Fellow. At MicroNano Laboratory (http://micronano.itu.edu.pk/), he has been working on reconfigurable intelligent surfaces (RIS), with the help of various EM simulation tools, under the supervision of Dr. Muhammad Zubair and Dr. Muhammad Qasim Mehmood. Recently, he has joined Faculty of ITU as a Teaching Fellow, in Fall 2023. His research interests include metasurfaces, communication systems, computer networks, and smart grids.

MUHAMMAD ZUBAIR (Senior Member, IEEE) received the Ph.D. degree in electronic engineering from the Politecnico di Torino, Italy, in 2015. From 2015 to 2017, he was a Postdoctoral Research Fellow with the SUTD-MIT International Design Centre, Singapore. In 2017, he joined the Information Technology University (ITU), as an Assistant Professor, where he was promoted to an Associate Professor, in 2021, and led the Applied and Computational Electromagnetic Group of MicroNao Laboratory. He has been a Visiting Faculty with Singapore University of Technology and Design (SUTD) and the King Abdullah University of Science and Technology (KAUST). He has published more than 180 journals and conference papers and two monographs/book chapters. His current research interests include applied and computational electromagnetics/photonics, fractional methods in the modeling and simulation of complex systems, microwave imaging for biomedical applications, electromagnetic metamaterials, reconfigurable intelligent surfaces for 6G applications, and AI-based electromagnetic design. He was a recipient of the Young Scientist Award by the International Union of Radio Science (URSI) and the Punjab Innovation Research Challenge Award. He serves on the editorial board of *PLOS One* and the *International Journal of Antennas and Propagation*. He has also served as an Associate Editor for IEEE Access and the *IET Microwaves, Antennas and Propagation*.

MARCO DI RENZO (Fellow, IEEE) received the Laurea (cum laude) and Ph.D. degrees in electrical engineering from the University of LAquila, Italy, in 2003 and 2007, respectively, and the Habilitation à Diriger des Recherches (Doctor of Science) degree from University Paris-Sud (currently Paris-Saclay University), Paris, France, in 2013. Currently, he is a CNRS Research Director (a Professor) and the Head of the Intelligent Physical Communications Group, Laboratory of Signals and Systems (L2S), CNRS and CentraleSupelec, Paris-Saclay University. Also, he is an Elected Member of the L2S Board Council; and a member of the L2S Management Committee, and the Admission and Evaluation Committee of the Ph.D. School on Information and Communication Technologies, Paris-Saclay University. He is a Founding Member and the Academic Vice Chair of the Industry Specification Group (ISG) on Reconfigurable Intelligent Surfaces (RIS) within the European Telecommunications Standards Institute (ETSI), where he served as the Rapporteur for the work item on communication models, channel models, and evaluation methodologies. He is a fellow of IET, EURASIP, and AAIA; an Academician of AIIA; an Ordinary Member of the European Academy of Sciences and Arts and the Academia Europaea; an Ambassador of the European Association on Antennas and Propagation; and a Highly Cited Researcher. Also, he holds the 2023 France-Nokia Chair of Excellence in ICT with Oulu University, Finland; and the Tan Chin Tuan Exchange Fellowship in engineering with Nanyang Technological University, Singapore. He was a Fulbright Fellow with the City University of New York, USA; a Visiting Professor with the Nokia Foundation, at Aalto University, Finland; and a Distinguished Visiting Fellow with the Royal Academy of Engineering, at Quens University Belfast, U.K. He is currently serving as a Voting Member for the Fellow Evaluation Standing Committee and as the Director of Journals of the IEEE Communications Society. His research awards include the 2021 EURASIP Best Paper Award, the 2022 IEEE COMSOC Outstanding Paper Award, the 2022 Michel Monpetit Prize conferred by the French Academy of Sciences, the 2023 EURASIP Best Paper Award, the 2023 IEEE ICC Best Paper Award, the 2023 IEEE COMSOC Fred W. Ellersick Prize, the 2023 IEEE COMSOC Heinrich Hertz Award, the 2023 IEEE VTS James Evans Avant Garde Award, the 2023 IEEE COMSOC Technical Recognition Award from the Signal Processing and Computing for Communications Technical Committee, the 2024 IEEE COMSOC Fred W. Ellersick Prize, the 2024 Best Tutorial Paper Award, and the 2024 IEEE COMSOC Marconi Prize Paper Award in Wireless Communications. He served as the Editor-in-Chief for IEEE COMMUNICATIONS LETTERS, from 2019 to 2023, and he is currently serving on the advisory board.

CHAU YUEN (Fellow, IEEE) received the B.Eng. and Ph.D. degrees from Nanyang Technological University, Singapore, in 2000 and 2004, respectively.

He was a Postdoctoral Fellow with Lucent Technologies Bell Laboratories, Murray Hill, in 2005. From 2006 to 2010, he was with the Institute for Infocomm Research, Singapore. From 2010 to 2023, he was with the Engineering Product Development Pillar, Singapore University of Technology and Design. Since 2023, he has been with the School of Electrical and Electronic Engineering, Nanyang Technological University, where he is currently the Provosts Chair in wireless communications and the Assistant Dean in Graduate College. He has four U.S. patents and published over 400 research articles at international journals.

Dr. Yuen received the IEEE Communications Society Leonard G. Abraham Prize, in 2024; the IEEE Communications Society Best Tutorial Paper Award, in 2024; the IEEE Communications Society Fred W. Ellersick Prize, in 2023; the IEEE Marconi Prize Paper Award in Wireless Communications, in 2021; the IEEE APB Outstanding Paper Award, in 2023; and the EURASIP Best Paper Award for *Journal on Wireless Communications and Networking*, in 2021. He serves as the Editor-in-Chief for *Springer Nature Computer Science*; an Editor for IEEE TRANSACTIONS ON VEHICULAR TECHNOLOGY, IEEE SYSTEM JOURNAL, and IEEE TRANSACTIONS ON NETWORK SCIENCE AND ENGINEERING, where he was awarded as an IEEE TRANSACTIONS ON NETWORK SCIENCE AND ENGINEERING Excellent Editor Award and a Top Associate Editor for TVT, from 2009 to 2015. He also served as the Guest Editor for several special issues, including IEEE JOURNAL ON SELECTED AREAS IN COMMUNICATIONS, *IEEE Wireless Communications Magazine*, *IEEE Communications Magazine*, *IEEE Vehicular Technology Magazine*, IEEE TRANSACTIONS ON COGNITIVE COMMUNICATIONS AND NETWORKING, and *Elsevier Applied Energy*. He is a Distinguished Lecturer of IEEE Vehicular Technology Society, Top 2% Scientists by Stanford University, and a Highly Cited Researcher by Clarivate Web of Science.